

The QCD deconfinement transition for heavy quarks and all baryon chemical potentials

Michael Fromm, Jens Langelage, Stefano Lottini, Owe Philipsen

*Institut für Theoretische Physik, Goethe-Universität Frankfurt,
Max-von-Laue-Str. 1, 60438 Frankfurt am Main, Germany*

E-mail:

fromm, langelage, lottini, philipsen@th.physik.uni-frankfurt.de

ABSTRACT: Using combined strong coupling and hopping parameter expansions, we derive an effective three-dimensional theory from thermal lattice QCD with heavy Wilson quarks. The theory depends on traced Polyakov loops only and correctly reflects the centre symmetry of the pure gauge sector as well as its breaking by finite mass quarks. It is valid up to certain orders in the lattice gauge coupling and hopping parameter, which can be systematically improved. To its current order it is controlled for lattices up to $N_\tau \sim 6$ at finite temperature. For nonzero quark chemical potentials, the effective theory has a fermionic sign problem which is mild enough to carry out simulations up to large chemical potentials. Moreover, by going to a flux representation of the partition function, the sign problem can be solved. As an application, we determine the deconfinement transition and its critical end point as a function of quark mass and all chemical potentials.

KEYWORDS: Strong-coupling expansion, Lattice gauge theory, Effective theory, Deconfinement, Heavy fermions, Finite density, Sign problem

Contents

1	Introduction	1
2	The effective action	2
2.1	Finite temperature $SU(N_c)$ Yang-Mills theory	2
2.2	Heavy fermions: LO hopping parameter expansion	5
2.3	Heavy fermions: beyond leading order	7
2.4	Observables	8
2.5	Flux representation and numerical simulation	9
3	The deconfinement transition for heavy quarks	11
3.1	Zero baryon density	11
3.2	Finite baryon density	16
3.3	Imaginary chemical potential	19
3.4	The deconfinement transition for all parameter values	20
4	Conclusions	21

1 Introduction

The determination of the QCD phase diagram is a fully non-perturbative problem, because QCD is strongly coupled on the scales relevant to heavy ion collisions and astrophysics, i.e. for temperatures $T \lesssim 400$ MeV and baryon chemical potentials $\mu_B \sim 0 - 3$ GeV. On the other hand, a direct first principles approach by Monte Carlo simulations of lattice QCD is ruled out by the sign problem, with a complex fermion determinant for quark chemical potential $\mu = \mu_B/3 \neq 0$ prohibiting importance sampling. Existing workarounds based on reweighting, Taylor expansions in μ/T or simulations at imaginary chemical potential followed by analytic continuation all introduce additional systematic errors and require $\mu/T \lesssim 1$ in order to be valid. For an elementary introduction, see [1]. As a consequence, the QCD phase diagram remains largely unknown.

This situation warrants additional investigations by effective theory methods. Popular approaches are based on models which share the chiral and/or the $Z(3)$ -symmetry with QCD, such as PNJL models, Polyakov loop + quark meson models, sigma models etc. For recent discussions and references, see [2–4]. Other approaches start from QCD directly and employ Dyson-Schwinger [5] or functional renormalisation group methods [6], using particular truncations. A general difficulty with effective theories is to assess the associated systematic errors.

Recently, a systematic derivation of a 3d centre-symmetric effective theory for finite temperature $SU(N_c)$ Yang-Mills by means of a strong coupling expansion has been presented, followed by numerical simulations [7]. The effective theory depends on Polyakov

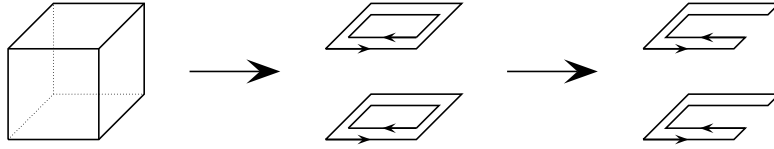


Figure 1. Integration of the cube consisting of 6 plaquettes. In the middle, four spatial link variables have been integrated over and we end up with two doubly occupied plaquettes. Integrating two of the remaining U_i yields the structure on the right which gives a factor $[\text{Tr}(U^\dagger U)]^2 = N_c^2$.

loop variables only, and can be improved order by order. Its couplings $\lambda_i = \lambda_i(\beta, N_\tau)$ are calculable functions of the lattice gauge coupling β and the temporal lattice extent N_τ of the original finite temperature lattice theory. The influence of the various couplings can be checked. Remarkably, the effective theory with only one coupling reproduces the correct order of the deconfinement transition for $SU(2)$, $SU(3)$, and moreover permits a quantitative estimate of the critical couplings $\beta_c(N_\tau)$ for sufficiently fine lattices, such that a continuum extrapolation of T_c is feasible.

In this work we extend the effective theory to include heavy but dynamical fermions of mass M by means of a hopping parameter expansion. This theory permits to explore the phase diagram of QCD with heavy quarks in the (M, T, μ) parameter space. A similar approach to the fermionic sector was taken in [8], which however left the gauge sector in the original 4d form. Here we extend the effective fermionic action to order κ^6 in the hopping expansion. As we shall see, for $\mu = 0$ we once again obtain good agreement with full 4d simulations where such results exist. However, the 3d effective theory allows for a solution to the sign problem and to explore the full range of quark chemical potentials with numerical ease, making contact with the region of asymptotically large chemical potentials. As a first application of the theory, we map out the entire deconfinement critical surface delimiting the region of first-order deconfinement transitions in the $(M_{u,d}, M_s, \mu)$ parameter space.

In Section 2 we derive the effective theory and discuss its numerical evaluation, comparing a direct simulation with Polyakov loop degrees of freedom with that of a flux representation free of the sign problem. Section 3 is devoted to the study of the QCD deconfinement transition, followed by our conclusions and a discussion of further prospects in Section 4.

2 The effective action

2.1 Finite temperature $SU(N_c)$ Yang-Mills theory

For the paper to be self-contained and to fix the notation, we briefly summarise the main formulae for the $SU(N_c)$ pure gauge case [7]. Starting point is the partition function for the 4d Euclidean Yang-Mills theory with Wilson gauge action,

$$\begin{aligned}
 Z &= \int [dU_0] [dU_i] \exp[-S_g] , \\
 -S_g &= \frac{\beta}{2N_c} \sum_p \left(\text{Tr} U_p + \text{Tr} U_p^\dagger \right) , \quad \beta = \frac{2N_c}{g^2} .
 \end{aligned} \tag{2.1}$$

Finite temperature and the bosonic degrees of freedom imply the use of periodic boundary conditions in the compactified time direction with N_τ slices, setting the temperature scale

by the lattice spacing a , $T = 1/(aN_\tau)$. An effective three-dimensional theory emerges by integrating out the spatial degrees of freedom to get schematically

$$Z = \int [dU_0] \exp[-S_{\text{eff}}] ,$$

$$-S_{\text{eff}} = \ln \int [dU_i] \exp \left[\frac{\beta}{2N_c} \sum_p \left(\text{Tr } U_p + \text{Tr } U_p^\dagger \right) \right] \equiv \lambda_1 S_1 + \lambda_2 S_2 + \dots , \quad (2.2)$$

where the effective couplings λ_i are functions of the original parameters, $\lambda_i = \lambda_i(\beta, N_\tau)$. The introduction of the logarithm is convenient in order to employ the graphical cluster expansion, described e.g. in [9], which features only connected diagrams.

An important observation is that only graphs winding around the time direction are needed for the effective action. To see this, consider for example the integration of a cube shown in Fig. 1, which is a valid graph with non-vanishing contribution. Nevertheless, since it does not wind around the temporal lattice extent, the spatial link integrations suffice to remove *all* dependence on link variables. As a result, the cube contributes only as a function $f(\beta)$ to the effective partition function and hence cancels in expectation values or renormalised quantities such as the physical free energy density. This is true for all graphs which do not wind around the lattice.

After spatial integration, the interaction terms S_i in Eq. (2.2) then depend on the link variables only via Polyakov loops

$$L(\vec{x}) \equiv \text{Tr } W(\vec{x}) \equiv \text{Tr} \prod_{\tau=1}^{N_\tau} U_0(\vec{x}, \tau) . \quad (2.3)$$

Thus we transform the remaining path integration measure from temporal link variables to traced Polyakov loops, which introduces a reduced Haar measure denoted by e^V . We now consider $SU(3)$ and parametrise the measure by two angles of the diagonalised Polyakov loop, providing another factor e^V , so that at every spatial lattice site \vec{x} we have

$$L(\theta, \phi) = e^{i\theta} + e^{i\phi} + e^{-i(\theta+\phi)} , \quad V = \frac{1}{2} \ln \left(27 - 18|L|^2 + 8\text{Re}(L^3) - |L|^4 \right)$$

$$\longrightarrow \int \left[\prod_{\tau=1}^{N_\tau} dU_0(\tau) \right] = \int dW = \int dL e^V = \int_{-\pi}^{+\pi} d\theta \int_{-\pi}^{+\pi} d\phi e^{2V} . \quad (2.4)$$

In Eq. (2.2), we arrange the interaction terms in ascending order of their leading power of β in the strong coupling expansion of the corresponding effective coupling. The first such interaction term is between nearest neighbours $\langle ij \rangle$ in the fundamental representation and has the form

$$\lambda_1 S_1 = \lambda_1(\beta, N_\tau) \sum_{\langle ij \rangle} \left(L_i L_j^* + L_i^* L_j \right) , \quad (2.5)$$

where $L_i = L(\vec{x}_i)$. This leading order contribution comes from N_τ temporal plaquettes building a chain around the lattice, followed by spatial link integration. Knowledge of the relations $\lambda_i(\beta, N_\tau)$ allows to convert the critical couplings $\lambda_{i,c}$ of the three-dimensional

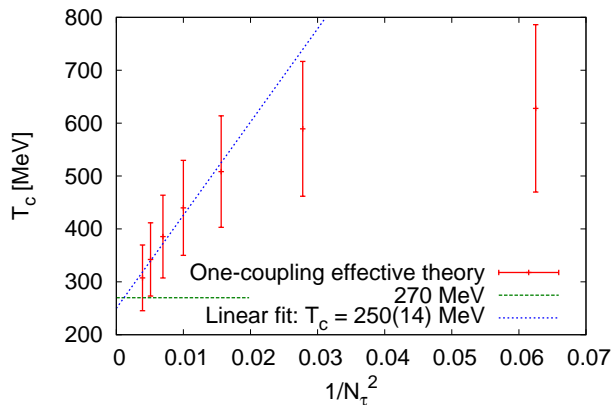


Figure 2. Critical temperature for the pure gauge deconfinement transition, extracted from the 3d effective theory, Eqs. (2.7, 2.6).

theory to those of the original theory. In particular, for the nearest neighbour coupling $\lambda_1(u, N_\tau)$ we find

$$\begin{aligned}
\lambda_1(u, 2) &= u^2 \exp \left[2 \left(4u^4 + 12u^5 - 18u^6 - 36u^7 \right. \right. \\
&\quad \left. \left. + \frac{219}{2}u^8 + \frac{1791}{10}u^9 + \frac{830517}{5120}u^{10} \right) \right], \\
\lambda_1(u, 4) &= u^4 \exp \left[4 \left(4u^4 + 12u^5 - 14u^6 - 36u^7 \right. \right. \\
&\quad \left. \left. + \frac{295}{2}u^8 + \frac{1851}{10}u^9 + \frac{1035317}{5120}u^{10} \right) \right], \\
\lambda_1(u, N_\tau \geq 5) &= u^{N_\tau} \exp \left[N_\tau \left(4u^4 + 12u^5 - 14u^6 - 36u^7 \right. \right. \\
&\quad \left. \left. + \frac{295}{2}u^8 + \frac{1851}{10}u^9 + \frac{1055797}{5120}u^{10} \right) \right], \quad (2.6)
\end{aligned}$$

where the character expansion coefficient $u = u(\beta) = \beta/18 + \dots$ of the fundamental representation is used instead of β due to better apparent convergence.

Altogether Eq. (2.2) has infinitely many couplings with loops in all irreducible representations, to all powers and at all distances. In the strong coupling region, the S_i are the more suppressed the higher the index i . In [7] we saw indeed that the influence of the next-to-nearest neighbour coupling as well as the adjoint coupling are negligible within the current level of accuracy when investigating the phase transition. We thus neglect these and higher-order correction terms in the following. Summing up powers of the nearest-neighbour interaction term [7], the effective theory for thermal Yang-Mills reads

$$Z_{\text{eff}} = \int \left(\prod_i dL_i e^{V_i} \right) \prod_{\langle ij \rangle} (1 + 2\lambda_1 \text{Re} L_i L_j^*). \quad (2.7)$$



Figure 3. Different terms occurring in the hopping expansion. Left: Plaquette. Middle: An example of a 6-link graph. Right: Generalised Polyakov loop, i.e. the loop winds around the temporal direction n times before the link variables are traced.

The deconfinement transition of Yang-Mills theory is reflected in an order-disorder transition of the effective theory. We determine the critical coupling to be $\lambda_{1,c} = 0.18805(2) \equiv \lambda_0$, cf. Sec.2.5¹, and, by inverting Eq. (2.6), extract the $\beta_c(N_\tau)$ which agree with full 4d Monte Carlo results within better than 10% accuracy up to $N_\tau = 16$. Using the non-perturbative beta-function for $a(\beta)$ provided in [10], these can then be converted to deconfinement temperatures, as shown in Fig. 2. Note that all points stem from a single determination of $\lambda_{1,c}$ in the effective theory. A continuum extrapolation in a^2 , i.e. $1/N_\tau^2$, is feasible and predicts a deconfinement transition of $T_c = 250(14)(50)$ MeV. The second, systematic error is taken as the difference between the $\mathcal{O}(u^{10})$ and $\mathcal{O}(u^9)$ in Eq. (2.6). Encouraged by this result, we now proceed to extend the effective theory to include heavy Wilson fermions.

2.2 Heavy fermions: LO hopping parameter expansion

Heavy fermions are conveniently introduced using the hopping parameter expansion, which is described in [9] at zero temperature and discussed in [11, 12] for finite temperature. The quark part of the action for N_f mass-degenerate flavours with masses $M_f = M$ can then be written as

$$-S_q = -N_f \sum_{l=1}^{\infty} \frac{\kappa^l}{l} \text{Tr} H[U]^l, \quad \kappa = \frac{1}{2aM + 8}, \quad (2.8)$$

with the hopping matrix

$$H[U]_{y,x} \equiv \sum_{\pm\nu} \delta_{y,x+\hat{\nu}} (1 + \gamma_\nu) U_\nu(x), \quad \gamma_{-\nu} = -\gamma_\nu. \quad (2.9)$$

Thus each hop to a neighbouring lattice site gives a power of the hopping parameter κ . The quark chemical potential μ is introduced as usual by a factor $e^{a\mu}$ ($e^{-a\mu}$) multiplying link variables in positive (negative) time direction [13]. The Kronecker delta in Eq. (2.9) requires that the graphs in the hopping expansion be closed. In Fig. 3 we show several graphs appearing in the hopping expansion. As an example and in order to establish a physical mass as reference scale, we calculate the pion mass to leading orders,

$$aM_\pi = -2 \ln(2\kappa) - 6\kappa^2 - 54\kappa^4 - 24\kappa^2 \frac{u}{1-u} + \mathcal{O}(\kappa^6, \kappa^2 u^5). \quad (2.10)$$

At finite temperature there are also graphs with a nontrivial winding number, such as generalised Polyakov loops

$$\text{Tr} W^n(\vec{x}) \equiv \text{Tr} \left(\prod_{\tau=1}^{N_\tau} U_0(\vec{x}, \tau) \right)^n, \quad 1 \leq n \leq \infty, \quad (2.11)$$

¹The slight discrepancy between λ_0 and the $\lambda_{1,c}$ of [7] is due to finite-size effects, as in the latter determination system sizes only up to $N_s = 14$ were employed.

winding around the lattice n times before being traced, cf. Fig. 3 (right).

We obtain the effective action from the full partition function in the same way as in pure gauge theory,

$$\begin{aligned} Z &= \int [dU_0][dU_i] \exp[-S_g - S_q] = \int [dU_0] \exp[-S_{\text{eff}}] , \\ -S_{\text{eff}} &= \ln \int [dU_i] \exp[-S_g - S_q] . \end{aligned} \quad (2.12)$$

We are now faced with a double series expansion in $u(\beta)$ and κ , i.e. the effective couplings depend on both parameters and N_τ . Furthermore, quarks of finite mass lead to terms in the action which explicitly break the $Z(3)$ symmetry present in the pure gauge case. The effective action may then be written as

$$-S_{\text{eff}} = \sum_{i=1}^{\infty} \lambda_i(u, \kappa, N_\tau) S_i^s - 2N_f \sum_{i=1}^{\infty} \left[h_i(u, \kappa, \mu, N_\tau) S_i^a + \bar{h}_i(u, \kappa, \mu, N_\tau) S_i^{a,\dagger} \right] . \quad (2.13)$$

The λ_i are defined as the effective couplings of the $Z(3)$ -symmetric terms S_i^s , whereas the h_i multiply the asymmetric terms S_i^a . Consequently, only the latter are μ -dependent and we recover pure gauge theory for $\kappa \rightarrow 0$, as in the full theory. We have not included the factor $2N_f$ in the definition of the h_i , since there are N_f mass-degenerate quarks with 2 spin degrees of freedom, all giving the same contribution. The h_i and \bar{h}_i are related via

$$\bar{h}_i(u, \kappa, \mu, N_\tau) = h_i(u, \kappa, -\mu, N_\tau) . \quad (2.14)$$

We shall now derive combined strong coupling and hopping parameter expansions of these effective couplings, again by employing the graphical cluster expansion. Similar to the case of pure gauge theory, graphs contributing to the cluster expansion have to wind around the lattice in the compact τ -direction. Hence, the leading order contributions are Polyakov loops, and we can read off the leading-order couplings h_1 and \bar{h}_1 :

$$h_1 S_1^a + \bar{h}_1 S_1^{a,\dagger} = - \sum_{\vec{x}} \left[(2\kappa e^{a\mu})^{N_\tau} L(\vec{x}) + (2\kappa e^{-a\mu})^{N_\tau} L^*(\vec{x}) \right] \rightarrow h_1 = (2\kappa e^{a\mu})^{N_\tau} . \quad (2.15)$$

Note the minus sign which is due to the anti-periodic boundary conditions for fermions. It is possible to sum up the contributions of all generalised Polyakov loops oriented in positive time direction,

$$\exp \left\{ -2N_f \sum_{\vec{x}} \sum_{n=1}^{\infty} \left[\frac{(-1)^n}{n} (2\kappa e^{a\mu})^{nN_\tau} \text{Tr} (W^n) \right] \right\} = \prod_{\vec{x}} \det \left[1 + (2\kappa e^{a\mu})^{N_\tau} W \right]^{2N_f} , \quad (2.16)$$

using $\exp \text{Tr} \ln A \equiv \det A$, and similarly for the conjugate loop. The three-dimensional effective action to leading order in the hopping expansion then corresponds to the static approximation and reads

$$Z_{\text{eff}} = \int [dU_0] \left(\prod_{\langle ij \rangle} \left[1 + 2\lambda_1 \text{Re} L_i^* L_j \right] \right) \left(\prod_{\vec{x}} \det \left[\left(1 + h_1 W_{\vec{x}} \right) \left(1 + \bar{h}_1 W_{\vec{x}}^\dagger \right) \right]^{2N_f} \right) . \quad (2.17)$$

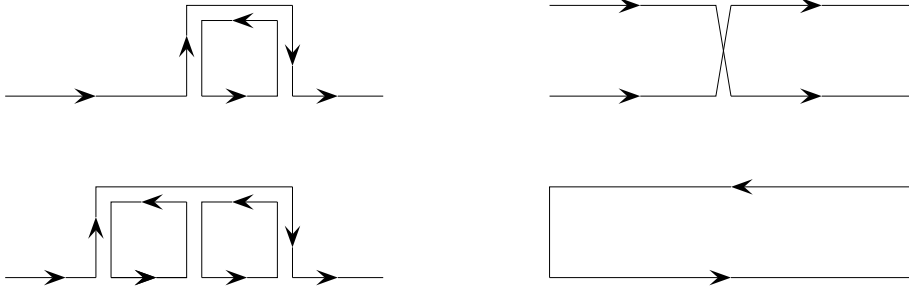


Figure 4. Left: Graphs reducing to Polyakov loops after spatial link integration resulting in $\mathcal{O}(\kappa^2 u^l)$ corrections, with $1 \leq l \leq N_\tau - 1$. Right: Graphs of $\mathcal{O}(\kappa^{2N_\tau+2})$, leading to interactions between Polyakov loops at distance a after spatial link integration.

2.3 Heavy fermions: beyond leading order

Corrections to the static approximation come from graphs that also contain spatial link variables. To order $\mathcal{O}(\kappa^4)$ there is the plaquette term, see Fig. 3 (left). Its contribution can be absorbed in the gauge term leading to a shift in β and hence to a κ -dependence of u ,

$$\beta \rightarrow \beta + 48N_f \kappa^4 \quad \Rightarrow \quad u(\beta) \rightarrow u(\beta, \kappa). \quad (2.18)$$

Higher-order graphs containing 6 and more links [9], for which Fig. 3 (middle) is an example, may be neglected to the orders to which we have calculated our effective couplings.

Next, we consider leading-order corrections to the winding graphs in the full (3+1)-dimensional action and observe their effect on the 3d effective theory, cf. Fig. 4. Graphs on the left lead to $\mathcal{O}(\kappa^2)$ corrections to the couplings h_1, \bar{h}_1 after spatial link integration. We have calculated the first correction to be

$$(2\kappa e^{a\mu})^{N_\tau} 6N_\tau \kappa^2 \sum_{l=1}^{N_\tau-1} u^l = (2\kappa e^{a\mu})^{N_\tau} 6N_\tau \kappa^2 \frac{u - u^{N_\tau}}{1 - u}, \quad (2.19)$$

by summing over $1 \leq l \leq N_\tau - 1$ possible attached plaquettes. As a result we get the higher order version of the effective coupling,

$$h_1 = (2\kappa e^{a\mu})^{N_\tau} \left(1 + 6N_\tau \kappa^2 \frac{u - u^{N_\tau}}{1 - u} + \dots \right). \quad (2.20)$$

Including all corrections up to $\mathcal{O}(u^n \kappa^m)$, with $n + m = 7$, we obtain

$$h_1(u, \kappa, N_\tau \geq 3) = (2\kappa e^{a\mu})^{N_\tau} \exp \left[6N_\tau \kappa^2 u \left(\frac{1 - u^{N_\tau-1}}{1 - u} + 4u^4 - 8\kappa^2 + 8\kappa^2 u + 4\kappa^2 u^2 - 4\kappa^4 \right) \right], \quad (2.21)$$

where we used the fact that terms $\sim N_\tau^2$ or higher can be resummed by writing the correction as an exponential. The graph in the lower right of Fig. 4 contributes a κ -dependent term to the already included nearest-neighbour interaction of Eq. (2.5). This

exemplifies how $\lambda_1(u, N_\tau)$ becomes $\lambda_1(u, \kappa, N_\tau)$. Note that these corrections do not change the form of the effective action Eq. (2.17).

By contrast, a graph that gives rise to a new term in the effective action is shown in the upper right corner of Fig. 4. Together with its oppositely oriented counterpart it implies interactions between Polyakov loops of the same orientation,

$$\begin{aligned} h_2 S_2^a + \bar{h}_2 S_2^{a,\dagger} &= \sum_{\langle ij \rangle} \left(h_2 L_i L_j + \bar{h}_2 L_i^* L_j^* \right), \\ h_2 &= (2\kappa e^{a\mu})^{2N_\tau} \frac{N_\tau \kappa^2}{N_c}, \quad \bar{h}_2 = (2\kappa e^{-a\mu})^{2N_\tau} \frac{N_\tau \kappa^2}{N_c}. \end{aligned} \quad (2.22)$$

However, the terms arising from both graphs on the right of Fig. 4 are parametrically of high order $\mathcal{O}(\kappa^{2N_\tau+2})$ and will thus be neglected along with even higher-order corrections.

For the remainder of this work we thus approximate thermal lattice QCD with heavy quarks by the effective theory Eq. (2.17) with the couplings h_1 of Eq. (2.21) and λ_1 of Eq. (2.6) with $u(\beta, \kappa)$ as in Eq. (2.18). Since we retain only one coupling of each sort, let us drop the index 1 and use the index i only to label lattice sites to lighten the notation. Finally, we rewrite Z_{eff} in a form more convenient for its numerical evaluation. A useful identity for the determinants is

$$\begin{aligned} \det(1 + hW) &= 1 + h\text{Tr}W + h^2\text{Tr}W^\dagger + h^3 = 1 + hL + h^2L^* + h^3, \\ \det(1 + \bar{h}W^\dagger) &= 1 + \bar{h}\text{Tr}W^\dagger + \bar{h}^2\text{Tr}W + \bar{h}^3 = 1 + \bar{h}L^* + \bar{h}^2L + \bar{h}^3. \end{aligned}$$

The heavy quark contribution per flavour and site \vec{x}_i then becomes

$$Q_i(h, \bar{h}) = \left[(1 + hL_i + h^2L_i^* + h^3)(1 + \bar{h}L_i^* + \bar{h}^2L_i + \bar{h}^3) \right]^2, \quad (2.23)$$

and the 3d effective theory for thermal QCD with heavy quarks reads simply

$$Z_{\text{eff}} = \int \left(\prod_i dL_i e^{V_i} Q_i^{N_f}(h, \bar{h}) \right) \prod_{\langle ij \rangle} (1 + 2\lambda \text{Re}L_i L_j^*). \quad (2.24)$$

In our numerical investigations we consider the partition function Eq. (2.24) for $N_f = 1$. Since the deconfinement transition at high temperature happens at small h , we can recover an arbitrary number of flavours by using the approximation

$$\det(1 + hW)^{N_f} \approx \exp(N_f hL), \quad h(N_f) \approx \frac{1}{N_f} h(N_f = 1). \quad (2.25)$$

2.4 Observables

In our numerical simulations we are interested in the phase structure. With a standard action linear in its couplings, one would typically construct observables using energy- and magnetisation-type fields defined as

$$E_{\text{lin}} = \frac{1}{3N_s^3} \sum_{\langle ij \rangle} 2\text{Re}L_i L_j^*, \quad Q_{\text{lin}} = \frac{1}{N_s^3} \left| \sum_i L_i \right| \quad (2.26)$$

on finite volumes $V = N_s^3$. In our case the non-linear action implied by Eq. (2.24) suggests to use a different definition, closer to what actually drives the dynamics of the system,

$$E = \frac{1}{\lambda} \frac{1}{3N_s^3} \sum_{\langle ij \rangle} \log \left(1 + 2\lambda \text{Re} L_i L_j^* \right), \quad Q = \frac{1}{h} \frac{1}{N_s^3} \sum_i \log |Q_i|. \quad (2.27)$$

These are proportional to the previous definitions in the limit of small couplings (λ, h, \bar{h}) . For the finite size scaling analyses of the phase structure we used the susceptibility and the Binder cumulant constructed from the observables $O \in \{E, Q, E_{lin}, Q_{lin}\}$,

$$\chi_O = N_s^3 (\langle O^2 \rangle - \langle O \rangle^2), \quad B_{4,O} = \frac{\langle (O - \langle O \rangle)^4 \rangle}{\langle (O - \langle O \rangle)^2 \rangle^2}. \quad (2.28)$$

2.5 Flux representation and numerical simulation

The system described by the partition function Eqs. (2.17, 2.24) has a complex action and thus suffers from a sign problem for $h \neq \bar{h}$ ($\mu > 0$). In the simplified case where the local variables L_i take only values in the center, $L_i \in Z(3)$, i.e. the Potts model in a magnetic field, the sign problem can be solved by using a cluster algorithm [14] or a change of variables to obtain a flux representation [14, 15]. The latter approach can be generalised to the case of $SU(3)$ -valued Polyakov loops as was done in [16] for a related model. The flux representation of the partition function reads

$$Z_{\text{eff}}(\lambda, h, \bar{h}) = \sum_{\substack{\{n_b, m_b\} \\ \{n_i, m_i\}}} \prod_{b=(i,\mu)} W_b(n_b, m_b) \prod_i W_i(p_i, q_i, n_i, m_i). \quad (2.29)$$

As the $SU(3)$ -valued variables have been integrated out, the degrees of freedom are now local incoming and outgoing currents, $n_{i,\mu}, m_{i,\mu} = 0, 1$, respectively, located on the links connecting the site i and $i + \mu$, $\mu = \pm 1, \dots, \pm d$ as well as charges (or monomers) $n_i, m_i = 0, \dots, 4$ located on the sites of our cubic lattice. $W_b(n_b, m_b)$ is given by

$$W_b(n_b, m_b) = \begin{cases} 1, & \text{if } (n_b, m_b) = (0, 0) \\ \lambda, & \text{if } (n_b, m_b) = (0, 1) \text{ or } (1, 0) \\ 0 & \text{otherwise.} \end{cases} \quad (2.30)$$

If we rewrite the factor Q in Eq. (2.23) as a power series in L, L^* , $Q = \sum_{n,m} \xi_{n,m} L^n L^{*m}$ then the site weight W_i reads

$$W_i(p_i, q_i, n_i, m_i) = \xi_{n_i, m_i} \int dU L^{q_i + n_i} L^{*p_i + m_i} \geq 0, \quad (2.31)$$

where the last expression contains a traced $SU(3)$ link integral given in closed form in [17, 18]. W_i is positive for all $\mu \geq 0$ and the model no longer has a minus sign problem. Locally, this integration creates a Potts constraint $q_i + n_i = p_i + m_i \pmod{3}$, where

$$q_i = \sum_{\mu=\pm 1, \dots, \pm d} n_{i,\mu}, \quad p_i = \sum_{\mu=\pm 1, \dots, \pm d} m_{i,\mu}. \quad (2.32)$$

Thus, local currents are conserved modulo 3.

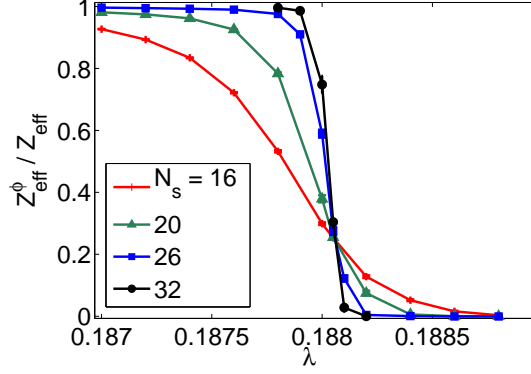


Figure 5. $Z_{\text{eff}}^{\phi}/Z_{\text{eff}}$ as a function of λ for the pure gauge case, crossing at $\lambda_0 \approx 0.18805$.

The partition function Eq. (2.29) is well-suited for an application of the worm algorithm [19] and its variants. To enable sampling of configurations in the presence of an external magnetic field ($h, \bar{h} \neq 0$) we implemented a variant of the algorithm presented in [20]. Having changed the degrees of freedom, the observables Eqs. (2.27) have to be re-expressed. The Polyakov loop and its complex conjugate are now given by

$$\frac{1}{V} \left\langle \sum_i L_i \right\rangle = \frac{1}{V} \frac{\partial}{\partial h} \ln Z \approx \langle n/h \rangle, \quad \frac{1}{V} \left\langle \sum_i L_i^{\dagger} \right\rangle \approx \langle m/\bar{h} \rangle, \quad (2.33)$$

where $\langle n \rangle$ and $\langle m \rangle$ denote the average number of monomers of either type. The relations become exact only in the limit $h, \bar{h} \rightarrow 0$, due to the non-exponential form of the quark part of expression Eq. (2.17). The quark density is given by

$$n_q = \frac{1}{VN_{\tau}} \frac{\partial}{\partial \mu} \ln Z = \frac{1}{VN_{\tau}} \left\langle \sum_i \frac{\partial_{\mu} W_i}{W_i} \right\rangle. \quad (2.34)$$

The worm algorithm relies on the sampling of the 2-pt function $G(i, j) = \langle L_i L_j^* \rangle$ rather than the partition function Eq. (2.29). $G(i, j)$ can be estimated during a worm update [19] as $G(i, j) = h(i, j)/Z$, where $h(i, j)$ corresponds to the histogram of configurations with the worm head (say L^*) at site j and its tail (L) at site i .

An observable more suitable for the flux representation is the free energy of an interface enforced in the broken phase by twisted boundary conditions in the e.g. z -direction, $L_{i+N_s \mathbf{e}_z} = e^{i\phi} L_i$ with $\phi = \frac{2\pi}{3}q$, $q = 0, 1, 2$. The partition function with twisted boundary conditions is

$$Z_{\text{eff}}^{\phi} = \sum_{\{n_x, m_x\}} e^{i\phi \sum_{x \in P} [n_z(x) - m_z(x)]} \prod_b W_b \prod_i W_i, \quad (2.35)$$

where $j_z = \sum_{x \in P} (n_z(x) - m_z(x))$ is the flux through the plane $P = \{\vec{x} \mid z = N_s - 1\}$. If we consider the case $h = \bar{h} = 0$, i.e. the model representing pure gauge theory, then the spontaneous breaking of centre symmetry is signalled by the ratio

$$\frac{Z_{\text{eff}}^{\phi}}{Z_{\text{eff}}} = \begin{cases} 1, & \text{for } T < T_c \\ 0, & \text{for } T > T_c. \end{cases} \quad (2.36)$$

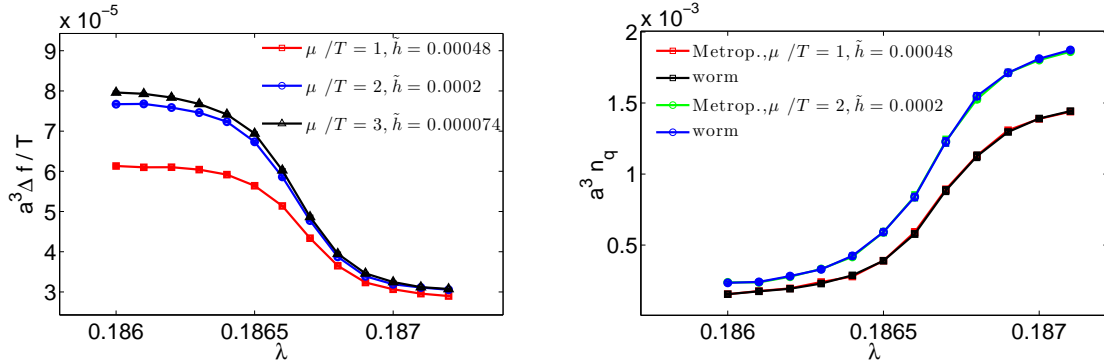


Figure 6. Left: Average sign, Eq. (2.37), of the fermion determinant in the effective theory in the vicinity of the critical point for various chemical potentials on a 24^3 lattice. Right: Quark density calculated with Z_{eff} from Eq. (2.24) (Metropolis) or Eq. (2.29) (worm) on 24^3 lattices.

In Fig. 5 we show $Z_{\text{eff}}^\phi/Z_{\text{eff}}$ as a function of λ for $\phi = 2\pi/3$. Since our model has a weak first order transition several volumes cross at the transition point $\lambda_0 = 0.18805(2)$.

On the other hand, compared to the full theory the sign problem in the standard representation of the effective theory, Eq. (2.24), is mild, similar to the case of the Potts model in an external field [21]. Using the modulus of the determinant in a Metropolis algorithm while reweighting in its phase, system sizes up to $N_s = 24$ for values of the chemical potential up to $\mu/T \sim 3$ can be reached, with a fully controlled average sign. To demonstrate this, we monitor the ratio of the full and phase quenched partition functions,

$$\langle \text{sign} \rangle_{||} = \frac{Z_{\text{eff}}}{Z_{\text{eff}}^{|}} = e^{-\frac{V}{T} \Delta f(\mu^2)}, \quad Z_{\text{eff}}^{|} : \text{phase quenched}. \quad (2.37)$$

The corresponding difference in free energy density is a volume-independent measure for the strength of the sign problem and is shown in Fig. 6 (left). Even for the largest system sizes to be used in our scaling analyses, the average sign remains significant and fully controlled up to large chemical potentials $\mu/T \sim 3$. This is corroborated by comparing a physical observable such as the quark density between the worm algorithm (without sign problem) and standard Metropolis algorithm with Polyakov loops and reweighting in the phase of the determinants. Fig. 6 (right) shows that no difference is discernible between the two ways of evaluating the observable.

We thus conclude that the sign problem can be fully controlled and even solved for our effective theory. Since the observables of interest are more readily accessible in the original degrees of freedom, we have mainly used the Metropolis algorithm for the following numerical simulations.

3 The deconfinement transition for heavy quarks

3.1 Zero baryon density

As a first application of the effective theory we investigate the deconfinement transition of QCD with heavy quarks as a function of quark mass and chemical potential. We begin by

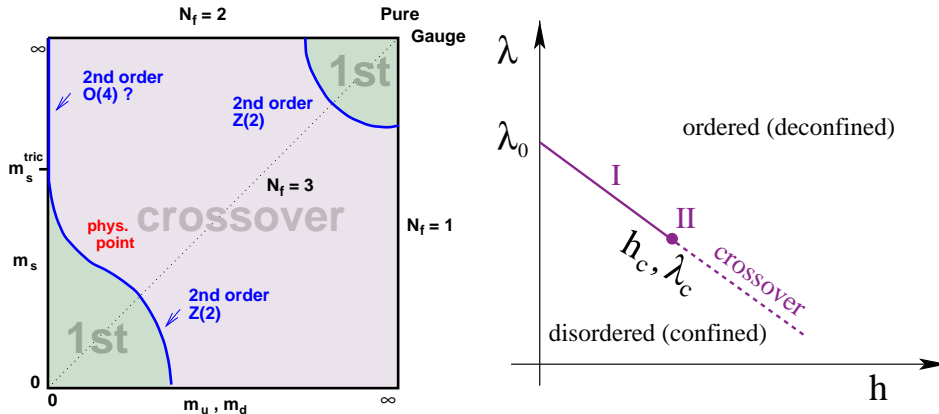


Figure 7. Schematic phase diagram for $\mu = 0$. Left: Nature of the QCD thermal transition for different quark masses. Right: Expected phase diagram for the effective theory corresponding to $\mu = 0$.

considering the case of zero baryon density, shown schematically in Fig. 7 (left). In the pure gauge limit, the deconfinement transition is of first order. Dynamical quarks at any fixed N_f break the global $Z(3)$ symmetry of the QCD action explicitly. As a consequence, the phase transition weakens with decreasing quark masses until it vanishes at a critical point. For still lighter quarks the deconfinement transition is an analytic crossover.

This behaviour is inherited by the effective theory. For a given N_f and $\mu = 0$, we have $h = \bar{h}$ and the effective theory has two couplings, (λ, h) . The first-order phase transition of the one-coupling theory extends to a first-order line with a weakening transition as h increases. Eventually the transition should vanish at a critical point, as sketched in Fig. 7 (right). These expectations are based on the known results of the 3d 3-state Potts model in an external field [14, 21], which shows the same symmetry breaking pattern. While the behaviour of the system in the vicinity of the critical point is dictated by the universality class, the location of the transition in parameter space, in particular the critical parameters where it changes its nature, are not. Hence, our investigation will give valuable additional information on QCD. Previous investigations to locate the critical heavy lattice quark mass have been made on coarse $N_\tau = 4$ lattices for $N_f = 1$ [22], and in [23] for several flavours.

In order to determine the phase diagram Fig. 7 (right), we follow a two-step procedure. First we determine the phase boundary, i.e. the pseudo-critical line $\lambda_{pc}(h)$ in the two-coupling space of the effective theory. In a second step, using dedicated finite size scaling analyses, we determine the order of the transition along that line, and in particular the location (λ_c, h_c) of the critical point. In order to accomplish the first task we fix the external field variable to the values $h = 0.0002 - 0.0012$ on lattice sizes $N_s = 10 - 24$, and then scan for the corresponding pseudo-critical coupling λ_{pc} . As indicators for the phase boundary we use maxima of susceptibilities and minima of Binder cumulants constructed from the observables given in Eqs. (2.26, 2.27). We extrapolate these to infinite volume using

$$\lambda_{pc}(h, N_s) = \lambda_{pc}(h) + c_1(h)/N_s^\alpha. \quad (3.1)$$

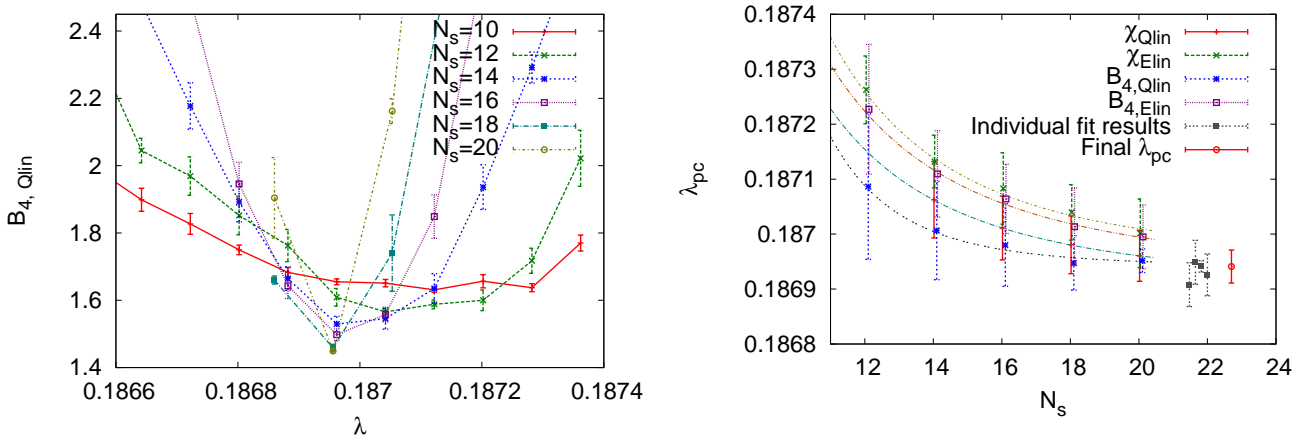


Figure 8. Pseudo-critical couplings for $h = \bar{h} = 0.0006$. Left: $B_{4,Qlin}$ on various volumes, the minima approach $\lambda_{pc}(h)$ in the thermodynamic limit. Right: Extrapolation of $\lambda_{pc}(h, N_s)$ from several observables to infinite volume.

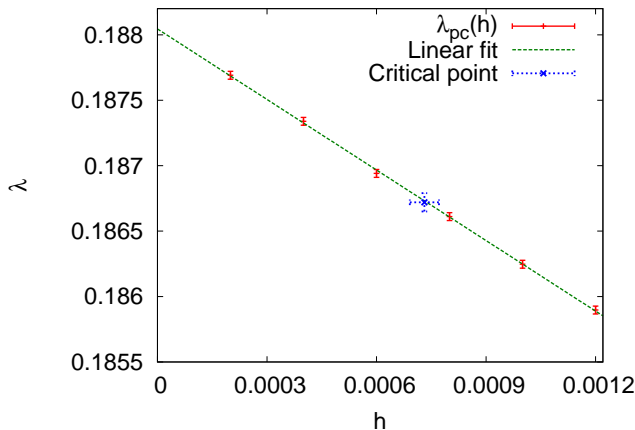


Figure 9. The pseudo-critical line or phase boundary in the thermodynamic limit. Also the critical point, Eq. (3.5), is shown.

For each coupling and system size we generated at least 10^5 configurations. Fig. 8 shows the minima of the Binder cumulant $B_{4,Qlin}$ for $h = 0.0006$ and the extrapolation of these values along with those of other observables. This results in the pseudo-critical line shown in Fig. 9. It is well described by a linear fit, due to the small magnitude of h and the argument given in [14]: along the line of first order transitions the free energy densities of the disordered (confined) phase and ordered (deconfined) phase are equal, $f_c(\lambda, h) = f_d(\lambda, h)$. Expanding both sides about the pure gauge transition, $(\lambda_0, h = 0)$, and noting that $\partial_h f_c = \langle L \rangle = 0$ in zero external field, we obtain

$$\lambda_{pc}(h) = \lambda_0 - a_1 h, \quad a_1 = \frac{\partial_h f_d}{\partial_\lambda (f_c - f_d)} \Big|_{(\lambda_0, 0)}. \quad (3.2)$$

A fit with $\chi^2 = 0.26$ yields $a_1 = 1.797(18)$ and $\lambda_0 = 0.18805(1)$ in very good agreement

	χ_Q	χ_Q	$B_{4,Q}$	$B_{4,Q}$
h_c	0.00073(1)	0.000739(1)	0.00071(1)	0.00072(2)
ν	0.63(1)	0.630 (fixed)	0.64(2)	0.630 (fixed)
γ/ν	2.00(1)	1.998(1)	–	–
f_0	16.88(4)	16.87(2)	1.58(1)	1.58(2)
f_1	−162(12)	−157(3)	7.6(8)	7.0(2)
f_2	460(60)	0 (fixed)	1(1)	0 (fixed)

Table 1. Critical end point h_c from fits to the scaling forms Eqs. (3.3) using data from $N_s = 20, 22, 24$ lattices (all with acceptable $\chi^2/\text{dof} < 1.5$). The known 3d Ising critical exponents are $\gamma/\nu = 1.962(3)$ and $\nu = 0.6302(1)$ [24].

with the estimate from the flux representation, see Fig. 5 and Sec. 2.5. An alternative approach to pin down the pseudo-critical line $\lambda_{pc}(h)$ would be to determine the principal axes \mathcal{E}, \mathcal{M} of the joint probability distribution $P(E, Q)$ of our variables. The critical line is then defined by a certain symmetry condition on $P(\mathcal{M})$, demanding the vanishing of the third moment $\langle \mathcal{M}^3 \rangle = 0$. We have checked explicitly around the critical point that the two approaches give consistent results.

In order to locate the critical end point of the first-order line and to establish its universality class, we study finite size scaling of the data taken along the pseudo-critical line. Close to criticality our observables should scale according to

$$\chi_Q = N_s^{\gamma/\nu} f_{\chi_Q}(x), \quad B_{4,Q} = f_{B_{4,Q}}(x), \quad x \equiv (h - h_c)N_s^{1/\nu} \quad (3.3)$$

with dimensionless scaling functions f_O , provided we move along the tangent $h_{pc}(\lambda)$. In the vicinity of the critical point the scaling functions may thus be expanded,

$$f_O(x) = f_0 + f_1 x + f_2 x^2 + \dots, \quad (3.4)$$

which is the form to which we fit our data. We simulated lattice sizes $N_s = 20, 22, 24$ with statistics of $\sim 7 \cdot 10^5$ configurations per parameter set and used binning analyses to control autocorrelations. For the susceptibility χ_Q , we find γ/ν consistent with the expected 3d Ising value, see Table 1 and Fig. 10. The fit was repeated fixing $f_2 = 0$, $\nu = 0.630$ (3d Ising), and varying the fit range $|x| < 0.01, 0.02, 0.03$, with an overall stable outcome. For the Binder cumulant $B_{4,Q}$, f_0 should approach a value characterising its universality class, ($f_0 = 1.604$ for 3d Ising [24]). The same fitting procedure as above was then applied to the $B_{4,Q}$ data for $N_s \geq 20$, with compatible values for h_c and f_0, ν , cf. Table 1. The collapse of the data onto a universal curve under the appropriate rescaling is also shown in Figs. 10, 11.

We are then ready to identify the critical point in Fig. 9 (right)

$$\left(\lambda_c = 0.18672(7), h_c = 0.000731(40) \right). \quad (3.5)$$

The values of λ_c, h_c can be converted into those of the couplings β_c, κ_c using Eqs. (2.6, 2.21). In order to compare with previous work, we approximate M_c/T with the relation,

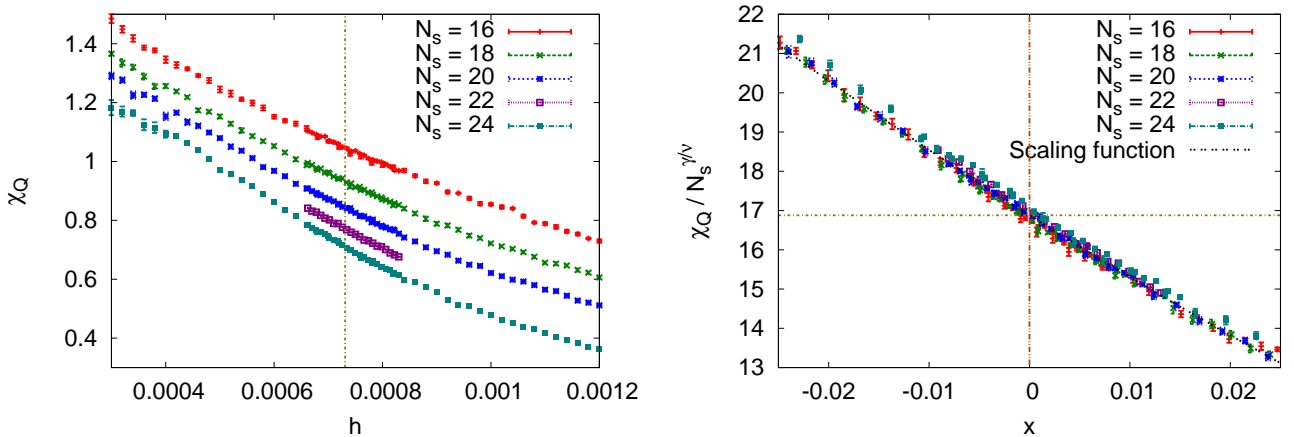


Figure 10. Left: χ_Q as a function of $h_{pc}(\lambda)$ for several volumes. Right: Same, now with rescaled axes, Eq. (3.3), to produce a collapsing curve described by the universal scaling function (see Table 1). The vertical line marks the critical h , the horizontal line is f_0 .

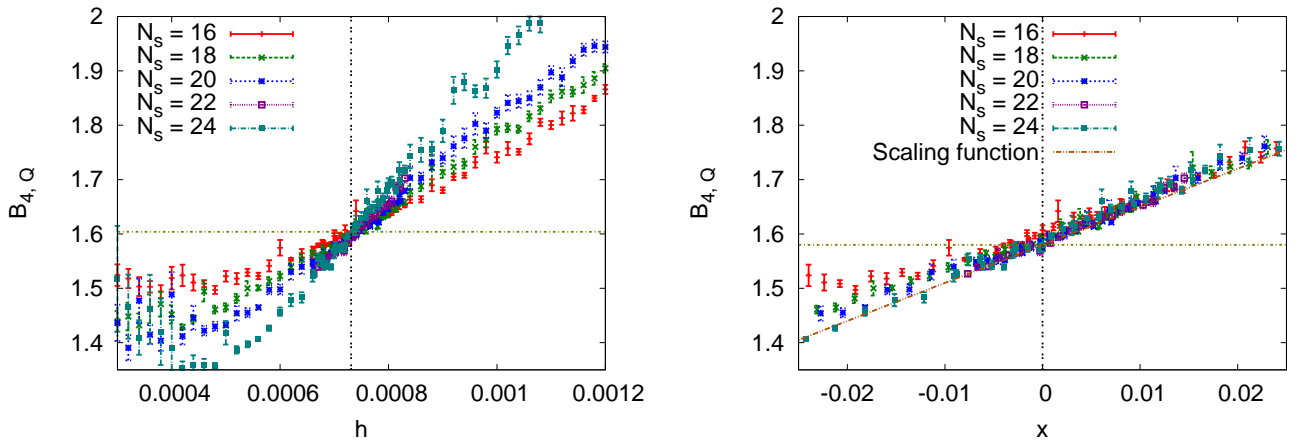


Figure 11. Left: $B_{4,Q}$ as a function of $h_{pc}(\lambda)$ for several volumes. The dashed horizontal line denotes the 3d Ising value 1.604 which is the approximate crossing value of the largest volumes $N_s = 20, 22, 24$, the vertical line marks the critical point. Right: Same, now with rescaled horizontal axis. The horizontal line marks $B_{4,Q}(0)$ as found numerically. Also shown is the universal scaling function obtained by the fit listed in Table 1, last column.

N_f	M_c/T	$\kappa_c(N_\tau = 4)$	$\kappa_c(4)$, Ref. [23]	$\kappa_c(4)$, Ref. [22]
1	7.22(5)	0.0822(11)	0.0783(4)	~ 0.08
2	7.91(5)	0.0691(9)	0.0658(3)	–
3	8.32(5)	0.0625(9)	0.0595(3)	–

Table 2. Location of the critical point for $\mu = 0$ and $N_\tau = 4$. The first two columns report our results (we used for consistency the leading-order relation Eq. 2.15), the last two compare with existing literature.

valid for heavy fermions to leading order in the hopping expansion [25],

$$\exp\left(-\frac{M}{T}\right) \simeq \frac{h}{N_f}. \quad (3.6)$$

The results are collected in Table 2 and are in reasonable agreement with the corresponding ones from simulations of 4d QCD with Wilson fermions [22, 23] at $N_\tau = 4$.

As in the case of pure gauge theory, our mapping of the critical effective couplings to those of QCD can in principle be done for any N_τ , thus providing predictions for larger N_τ which have not yet been simulated in 4d. However, before doing so we need to check how far we can trust our hopping parameter expansion. Fig. 12 (left) shows the predictions of the effective theory for $\kappa_c(N_\tau)$ to the orders κ^2 , κ^4 , resummed and unresummed. Also shown is the chiral critical hopping parameter, defined by the vanishing of the pion mass Eq. (2.10), and evaluated for the critical gauge couplings, $\kappa_{ch}(u_c(N_\tau))$. Since we are expanding around infinite quark masses, self-consistency requires $\kappa_c \ll \kappa_{ch}$. Whereas the leading order soon crosses the κ_{ch} line, the corrections are significantly below the leading order and the exponentiated versions further improve on this. Furthermore, literature tells us that $\kappa_{ch}(\beta = 0) = 0.25$ [26] and $\kappa_{ch}(\beta \rightarrow \infty) = 0.125$ [9], when all orders are taken into account. Hence, we conclude that $N_\tau = 6$ is the finest thermal lattice for which our κ_c is still significantly smaller than κ_{ch} evaluated at the same gauge coupling, and has not yet crossed the continuum-extrapolated κ_{ch} . This is corroborated by the pion mass $M_\pi(u_c, \kappa_c)$ evaluated at the critical point, shown in Fig. 12 (right). We observe that beyond $N_\tau \sim 6$ the differences between the non-trivial orders κ^2 and κ^4 grow larger, indicating that we leave the convergence region.

These findings are to be contrasted with $\beta_c(N_\tau)$ of the pure gauge effective theory, which are within a 10% range from the known 4d results up to $N_\tau = 16$. However, this is quite natural, since we have only three non-trivial orders in the hopping expansion, which are additionally truncated at a low order in u , compared to five orders in the strong coupling expansion. While we hope to extend our results to larger N_τ by going to higher orders in κ , at the moment we cannot take a continuum limit in the fermionic sector but consider our results valid up to $N_\tau \sim 6$.

Within this range of validity, we may now discuss the sensitivity of the deconfinement critical line in Fig. 7 (left) on the cut-off. The critical pion mass in units of temperature marking the boundary of the first order deconfinement region shrinks slightly from $N_\tau = 4$ to $N_\tau = 6$. This effect is even smaller in absolute units (T_c also decreases with increasing N_τ), in contrast to the critical pion mass evaluated on the chiral critical line, which shrinks by almost a factor of two [27]. Higher orders in the hopping expansion are needed for a definite statement in our case.

3.2 Finite baryon density

We now study the deconfinement transition at finite baryon density. For $\mu \neq 0$, we have $h \neq \bar{h}$ and need to consider the full parameter space of the effective theory, (λ, h, \bar{h}) . The diagram in Fig. 7 (right) turns three-dimensional, with a surface of first order phase transitions terminating in a critical line. Since we are interested in the change of the critical

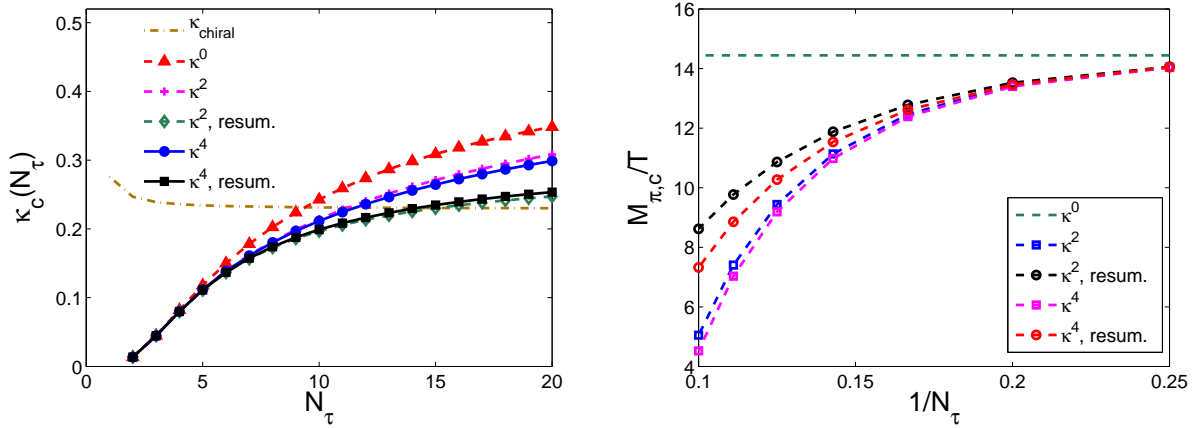


Figure 12. Critical hopping parameter $\kappa_c(N_\tau)$ (left) and critical pion mass $M_{\pi,c}(\kappa_c, u)/T$ (right) given by Eq. (2.10) for the end point of the $N_f = 1$ effective theory to different orders of the hopping expansion.

quark mass with chemical potential, we prefer to map out the critical line by fixing different chemical potentials and then scan for the critical κ . It is thus convenient to introduce the parameter

$$\tilde{h} \equiv h e^{-\mu/T} (= (2\kappa)^{N_\tau} \text{ to leading order in } \kappa) \quad (3.7)$$

and to present our data in the parameter space $(\lambda, \tilde{h}, \mu/T)$.

For our simulations, we used values of $\mu/T = 0.1, \dots, 3.0$ on three lattice sizes $N_s = 16, 20, 24$. Data were produced at a given set $(\lambda, \tilde{h}, \mu/T)$ close to the critical point and later reweighted to near-by values of the couplings. Over 700 k configurations were produced for each parameter set and lattice size. For each chemical potential, the pseudo-critical line $\lambda_{pc}(\tilde{h})$ was identified as the curve of local minima in $B_{4,Q}$, Fig. 13, showing again linear behaviour as already observed for $\mu = 0$. Indeed we can repeat the steps leading to Eq. (3.2), this time setting $f_c(\lambda, \tilde{h}, \mu/T) = f_d(\lambda, \tilde{h}, \mu/T)$ along the first order line. For small fields \tilde{h} we expand about the Yang-Mills limit $(\lambda, \tilde{h}, \mu/T) = (\lambda_0, 0, 0)$ and obtain

$$\lambda_{pc}(\tilde{h}, \mu/T) = \lambda_0 + a_1(\mu/T)\tilde{h}, \quad a_1 = \left. \frac{2\partial_h f_d}{\partial_\lambda (f_c - f_d)} \right|_{(\lambda_0, 0, 0)} \cosh(\mu/T). \quad (3.8)$$

Fitting to this form ($\chi^2/\text{dof} \simeq 1.5$) gives an intercept $\lambda_0 = 0.18802(2)$ consistent with λ_0 in Eq. (3.2) and a slope

$$a_1(\mu/T) = C \cosh(\mu/T) \quad (3.9)$$

with $C = -1.814(3)$, which is compatible with Eq. (3.2).

As for $\mu = 0$, the critical points $\lambda_c(\tilde{h}_c(\mu/T), \mu/T)$ can be found again by evaluating $B_{4,Q}$ along each μ -line on different volumes. To avoid doing the entire finite size analysis for all parameter sets we take the critical point as the crossing of the $N_s = 24$ data with the theoretical value of 1.604. The difference between this procedure and the crossing of individual volumes serves as an estimate for finite size effects. On the resulting critical

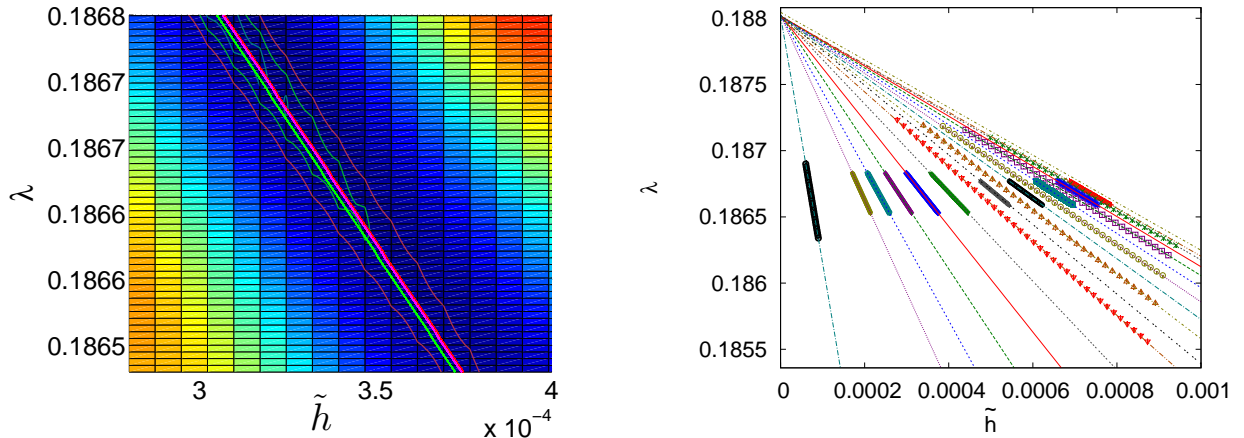


Figure 13. Left: Binder cumulant $B_{4,Q}(\tilde{h}, \lambda)$ for chemical potential $\mu/T = 1.4$ ($N_s = 24$). The thick straight lines mark the locus of the minima at $N_s = 16, 24$, the surrounding contour lines correspond to the values 1.58, 1.64, 1.74. Right: Transition lines $\lambda_{pc}(\tilde{h}, \mu/T)$ for several values of μ/T between 0 (top) and 3.0 (bottom).

line, $\lambda_c(\tilde{h}_c(\mu/T), \mu/T)$ shows only weak dependence on μ/T within our statistical accuracy and varies around $\lambda_c \approx 0.18670(5)$. Note that this remains true even for large μ/T , as we shall see in Eq. (3.12).² We exploit this behaviour to find a simple parametric description of the critical line in terms of the parameters of the original QCD action. Setting $\Delta\lambda = \lambda_c(\mu/T) - \lambda_0 \approx \text{const}$, we may rewrite Eq. (3.8) at the critical point for fixed μ/T as

$$\tilde{h}_c(\mu/T) = \frac{\Delta\lambda}{C \cosh(\mu/T)} \equiv \frac{D}{\cosh(\mu/T)}. \quad (3.10)$$

A fit of all $\mu > 0$ data to Eq. (3.10) with only D as parameter performs indeed very well, yielding $D = 0.00075(1)$ with $\chi^2/\text{dof} = 0.6$. The corresponding $h_c(\mu = 0) = D$ is also compatible with our findings at $\mu = 0$. The resulting curve is shown in Fig. 14 (right). While the data seem to be reasonably well described by the Ansatz Eq. (3.10), a systematic underestimation at small μ/T hints towards a more complex law. Indeed our curve is the result of a first order expansion in (λ, h, \tilde{h}) , Eq. (3.8), followed by the approximation $\Delta\lambda \approx \text{const}$ and a fit over the whole μ -range.

On the other hand, asymptotically large chemical potentials in the original lattice QCD are described by the limit

$$\kappa \rightarrow 0, \mu \rightarrow \infty \text{ with } \kappa e^{\mu/T} = \text{const}. \quad (3.11)$$

The corresponding effective theory has two parameters, $(\lambda, h, \tilde{h} = 0)$. The critical point in this case is easily found by the same techniques,

$$(\lambda_c, h_c)|_{\tilde{h}=0} = (0.18668(2), 0.00142(2)). \quad (3.12)$$

²Interestingly, the same observation is made in the 3d Potts model, where the spin coupling as a function of the external fields is nearly constant along the critical line, e.g. [21].

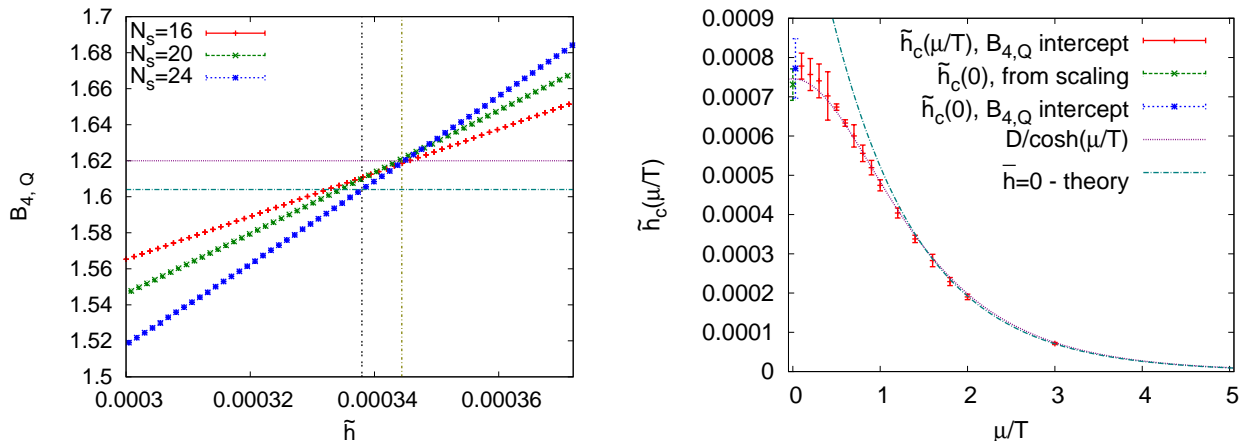


Figure 14. Left: $B_{4,Q}$ for different system sizes along the pseudo-critical line for $\mu/T = 1.4$. The horizontal lines mark the thermodynamic limit value of $B_{4,Q}$ at criticality and the actual value of the crossing. Right: Critical line $\bar{h}_c(\mu/T)$; the curves are the fit to the $\cosh^{-1}(\mu/T)$ behaviour, Eq. (3.10), and the large- μ asymptotic limit, Eq. (3.11). The separate $\mu = 0$ determination is compatible with these findings.

Using the leading order expression for h , Eq. (2.15), this gives the $\bar{h} = 0$ -critical curve $\bar{h}_c(\mu/T)$ which is also plotted in Fig. 14. Already for $\mu/T \gtrsim 1.5$ the data are accurately described by the asymptotic density limit. Taking this result together with the curve Eq. (3.10) we thus have obtained a description of the $N_f = 1$ deconfinement critical line for all real chemical potentials!

3.3 Imaginary chemical potential

The QCD phase transitions and its limiting critical surfaces possess an analytic continuation to negative μ^2 , or imaginary chemical potentials, $\mu = i\mu_i$. This has been exploited previously [28, 29], since in this case the fermion determinant is real positive and properties of the critical surfaces can be calculated without sign problem. In particular, the deconfinement critical surface is expected to terminate in a tricritical line at $\mu_i/T = \pi/3$ [30]. This value of imaginary chemical potential marks the boundary to an adjacent $Z(3)$ centre-sector of the partition function [31]. Our effective theory correctly reflects the centre symmetry and its breaking in QCD, and hence the related phase structure. In this section we explicitly compute the continuation of the critical quark masses, i.e. the deconfinement critical surface, from $\mu = 0$ to $\mu/T = i\pi/3$.

Now also the fermionic part of our effective theory, Q_x , is explicitly real. Numerically we follow the same approach as for real μ , choosing values of $\mu_i/T = 0.1 - \frac{\pi}{3}$, followed by determinations of the pseudo-critical and critical couplings. We observe increasing numerical difficulties as μ_i approaches the boundary to the next centre sector. Moving along the critical line towards the Roberge-Weiss tricritical point, a crossover between 3d Ising and tricritical scaling sets in, thus obscuring the finite size analysis and demanding ever larger volumes. Controlled errors were obtained up to $\mu_i/T \lesssim 0.8$.

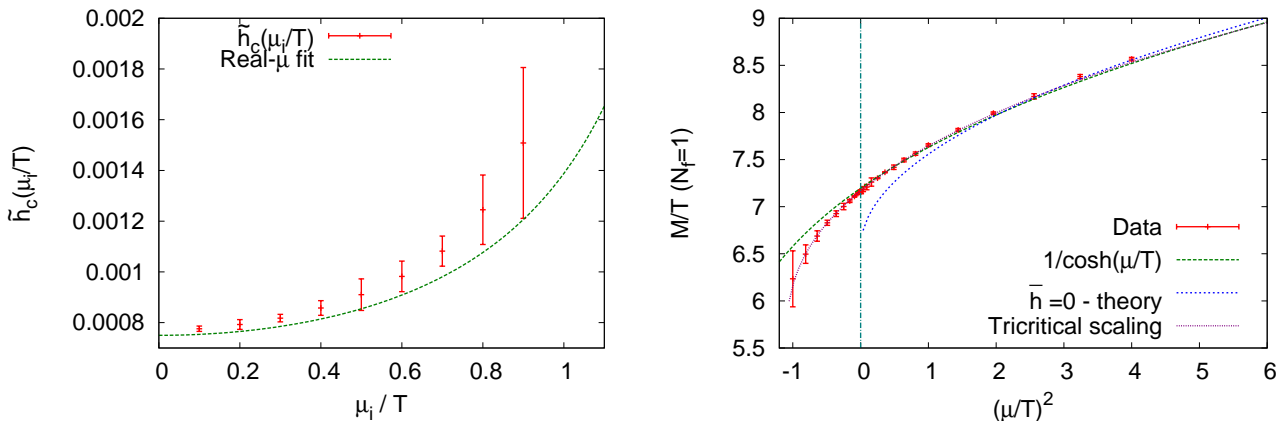


Figure 15. Left: Critical coupling \tilde{h}_c for imaginary chemical potential μ_i , also shown is the analytic continuation of the real- μ fit to Eq. (3.10). Right: M_c/T for $N_f = 1$ at both imaginary and real chemical potential. The curves represent Eq. (3.10) (and its analytical continuation), the large- μ asymptote from Eq. (3.11), and the tricritical scaling, Eq. (3.13).

With increasing μ_i , the endpoint of the corresponding first order line is shifted towards higher $\tilde{h}_c(\mu_i/T)$. The resulting critical line is shown in Fig. 15 (left). The pseudo-critical lines $\lambda_{pc}(\tilde{h}, \mu_i/T)$ develop a curvature for increasing μ_i and thus invalidate a first order expansion of the free energy as done in Eq. (3.8). As a consequence, an analytic continuation of the real- μ fit Eq. (3.10) to imaginary chemical potential leads to a less satisfying description of the data. However, we may put real and imaginary μ data together and plot M_c/T as in Fig. 15 (right). (To convert $\tilde{h} \rightarrow M$, we use Eq. (3.6), with $h_c e^{-\mu/T}$ instead of simply h_c). It was demonstrated in [30] for the Potts model and strong coupling QCD that the critical quark mass at imaginary chemical potential is governed by tricritical scaling, with a scaling region extending all the way to real μ . We thus attempt the corresponding two-parameter fit to tricritical scaling,

$$\frac{M_c}{T} \left(\frac{\mu^2}{T^2} \right) = \frac{M_{tric}}{T} + K \left[\left(\frac{\pi}{3} \right)^2 + \left(\frac{\mu}{T} \right)^2 \right]^{2/5}, \quad (3.13)$$

which is shown in Fig. 15 (right). Fitting solely the region $\mu^2 < 0$ yields $K = 1.55(3)$, and $M_{tric}/T = 5.56(3)$ with $\chi_{red}^2 = 0.13$. Different numbers of flavours can be re-introduced as for $\mu = 0$, obtaining

$$\frac{M_{tric}}{T} = \{5.56(3), 6.25(3), 6.66(3)\}, \text{ for } N_f = \{1, 2, 3\}. \quad (3.14)$$

Remarkably, the scaling function correctly describes the data up to large real chemical potentials, in fact well into the region described by asymptotically large μ .

3.4 The deconfinement transition for all parameter values

Collecting our results from the previous sections, we can describe the entire deconfinement critical surface from imaginary chemical potentials all the way to the large- μ limit. Moreover, we have a simple and accurate parametrisation of the surface by stitching together

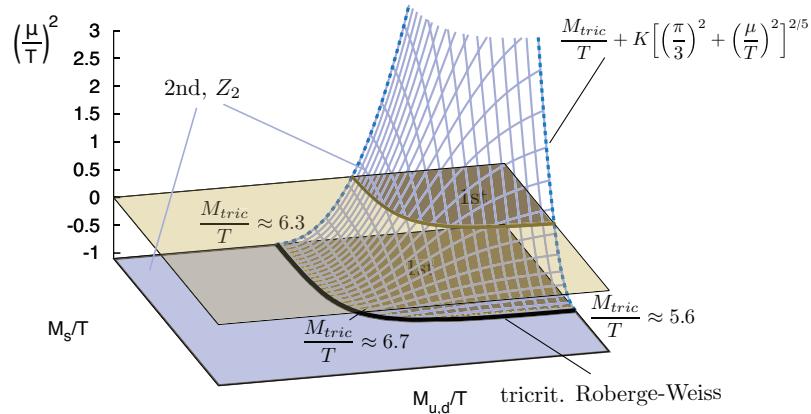


Figure 16. The deconfinement critical surface of QCD with heavy quarks.

tricritical scaling, the $\cosh^{-1}(\mu/T)$ -behaviour for moderate μ and the curve describing the asymptotic limit. Converting to a $(2+1)$ -flavour setting with different masses $M_{u,d} \neq M_s$, we may plot the critical surface for the upper-right corner of the Columbia plot (Fig. 7, left). The final result is shown in Fig. 16. To convert to quark mass M/T we used Eq. (3.6), valid to leading order in the hopping expansion and for small $N_\tau \lesssim 6$.

By fixing the quark content, e.g. $N_f = 2$, we can similarly draw the full deconfinement transition in $(\frac{\mu}{T}, \frac{M_\pi}{2T}, \frac{T}{T_0})$ -space, with T_0 the pure gauge transition temperature. Since our quarks are very heavy, they give negligible contribution to the beta-function and we use again the Sommer parametrisation from pure gauge theory [10] to set the scale. As for $\mu = 0$, our results are only controlled up to $N_\tau \sim 6$. This yields the phase diagrams in Fig. 17. The deconfinement temperature for quarks of large but finite mass is almost μ -independent and smoothly approaches a constant value as expected for the quenched limit of infinitely heavy quarks.

4 Conclusions

We have applied strong coupling and hopping parameter expansions to lattice QCD with Wilson fermions at finite temperature and quark chemical potential. The resulting three-dimensional effective theory depends solely on traced Polyakov loops, i.e. complex scalars, with its couplings given analytically in terms of the original parameters of the theory, β, κ, N_τ . This leads to a considerable simplification of numerical simulations. In the pure gauge limit we know five non-trivial orders in the strong coupling expansion, and the resulting critical parameters are valid up to $N_\tau \sim 16$, enabling a continuum extrapolation of T_c . However, the hopping expansion has only been performed up to order κ^6 , such that our theory with quarks is only robust to $N_\tau \sim 6$ so far. Nevertheless, this corresponds to finer lattices than have been directly simulated in the heavy quark regime at the time of writing, and moreover offers intriguing features absent in the full 4d theory. The sign problem is mild enough to directly simulate the model, and can be solved completely within a flux representation of the partition function. Hence a numerical study for all

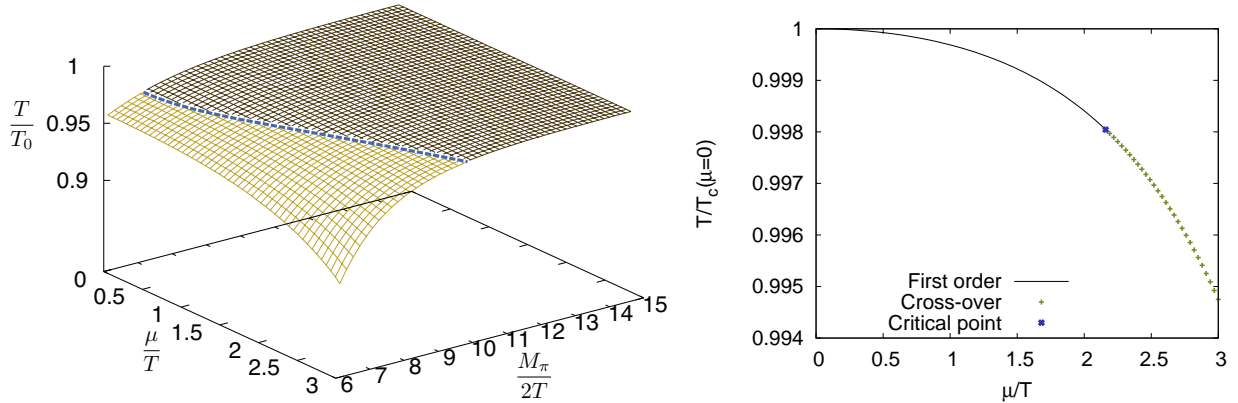


Figure 17. Left: Phase structure of the theory in $(\frac{\mu}{T}, \frac{M_\pi}{2T}, \frac{T}{T_0})$ -space, for $N_f = 2$ and $N_\tau = 6$. Above the surface the theory is deconfined. The critical line (dashed) separates the cross-over (light) and the first-order surface (dark). Right: Phase diagram of the theory for $M_\pi/(2T) \simeq 8.9$, $N_f = 2$ and $N_\tau = 6$.

values of the chemical potential is feasible. We have demonstrated this by computing the entire deconfinement critical surface. While this region of the QCD parameter space is far from the physical parameter values, we have presented the first full QCD lattice calculation involving an arbitrary chemical potential. Furthermore, our results may serve as benchmarks for analytic approaches, which can easily tune the quark masses. There are many ways forward from here. As a next step, it would be interesting to study the cold and dense regime within the current effective theory. Improvements on the present state can be made by either carrying the analytic calculations to higher order, including additional couplings, or non-perturbatively by inverse Monte Carlo methods along the lines of [32, 33]. Finally and most importantly, it is most interesting to explore the possibilities of a similar description for the light quark sector, either by extrapolating a higher-order hopping expansion or by an alternative formulation within the effective theory context.

Acknowledgements

This project is supported by the German BMBF under contract number 06MS9150 and by the Helmholtz International Center for FAIR within the framework of the LOEWE program launched by the State of Hesse.

References

- [1] O. Philipsen, arXiv:1009.4089 [hep-lat].
- [2] K. Fukushima, PoS **CPOD2009** (2009) 016.
- [3] W. Weise, Prog. Theor. Phys. Suppl. **186** (2010) 390-403. [arXiv:1009.6201 [nucl-th]].
- [4] B.-J. Schaefer, arXiv:1102.2772 [hep-ph].
- [5] J. Lücker, C. S. Fischer, arXiv:1111.0180 [hep-ph].

- [6] L. M. Haas, J. Braun, J. M. Pawłowski, AIP Conf. Proc. **1343**, 459-461 (2011). [arXiv:1012.4735 [hep-ph]].
- [7] J. Langelage, S. Lottini and O. Philipsen, JHEP **1102** (2011) 057 [Erratum-ibid. **1107** (2011) 014]. [arXiv:1010.0951 [hep-lat]].
- [8] R. De Pietri, A. Feo, E. Seiler, I.-O. Stamatescu, Phys. Rev. **D76** (2007) 114501. [arXiv:0705.3420 [hep-lat]].
- [9] I. Montvay, G. Münster. Cambridge, UK: Univ. Pr. (1994) 491 p. (Cambridge monographs on mathematical physics).
- [10] S. Necco and R. Sommer, Nucl. Phys. B **622** (2002) 328.
- [11] J. Langelage, O. Philipsen, JHEP **1001** (2010) 089. [arXiv:0911.2577 [hep-lat]].
- [12] J. Langelage, O. Philipsen, JHEP **1004** (2010) 055. [arXiv:1002.1507 [hep-lat]].
- [13] P. Hasenfratz, F. Karsch, Phys. Lett. **B125** (1983) 308.
- [14] M. G. Alford, S. Chandrasekharan, J. Cox, U.J. Wiese, Nucl. Phys. **B602**, 61-86 (2001). [hep-lat/0101012].
- [15] J. Condeella, C. E. Detar, Phys. Rev. **D61**, 074023 (2000). [hep-lat/9910028].
- [16] C. Gattringer, Nucl. Phys. B **850**, 242 (2011). [arXiv:1104.2503 [hep-lat]].
- [17] K. E. Eriksson, N. Svartholm, B. S. Skagerstam, J. Math. Phys. **22**, 2276 (1981).
- [18] J. Carlsson, arXiv:0802.3409 [hep-lat].
- [19] N. Prokof'ev, B. Svistunov, Phys. Rev. Lett. **87**, 160601 (2001).
- [20] C. Gabriel, Diploma thesis, Graz (2002), <http://itp.tugraz.at/AG/AVP/thesis/>.
- [21] S. Kim, Ph. de Forcrand, S. Kratochvila, T. Takaishi, PoS(LAT2005) 166. [hep-lat/0510069].
- [22] C. Alexandrou, A. Boriçi, A. Feo, Ph. de Forcrand, A. Galli, F. Jegerlehner, T. Takaishi, Phys. Rev. **D60**, 034504 (1999). [hep-lat/9811028].
- [23] H. Saito *et al.* [WHOT-QCD Collaboration]. arXiv:1106.0974 [hep-lat].
- [24] Y. Deng and H. W. J. Blöte, Phys. Rev. **E68** (2003) 036125.
- [25] F. Green and F. Karsch, Nucl. Phys. B **238** (1984) 297.
- [26] N. Kawamoto, J. Smit, Nucl. Phys. B **192** (1981) 100.
- [27] Ph. de Forcrand, S. Kim, O. Philipsen, PoS **LAT2007** (2007) 178. [arXiv:0711.0262 [hep-lat]].
- [28] Ph. de Forcrand and O. Philipsen, JHEP **0701**, 077 (2007). [arXiv:hep-lat/0607017].
- [29] Ph. de Forcrand and O. Philipsen, JHEP **0811** (2008) 012. [arXiv:0808.1096 [hep-lat]].
- [30] Ph. de Forcrand, O. Philipsen, Phys. Rev. Lett. **105**, 152001 (2010). [arXiv:1004.3144 [hep-lat]].
- [31] A. Roberge and N. Weiss, Nucl. Phys. B **275**, 734 (1986).
- [32] C. Wozar, T. Kaestner, A. Wipf and T. Heinzl, Phys. Rev. D **76** (2007) 085004. [arXiv:0704.2570 [hep-lat]].
- [33] P. de Forcrand, A. Kurkela, A. Vuorinen, Phys. Rev. **D77** (2008) 125014. [arXiv:0801.1566 [hep-ph]].